Ecological Questions 36 (2025) 3: 127–135 http://dx.doi.org/10.12775/EQ.2025.029

Investigating the subsidence pattern of southwest Tehran using interferometric SAR time series

Behnam Asghari Beirami*, **Mohammadreza Seif**

Imam Hossein University, Tehran, Iran
*Corresponding author e-mail: behnam.asghari1370@gmail.com ;b_asghari@ihu.ac.ir

Received: 18 December 2024 / Accepted: 30 August 2025

Abstract. Due to drought and underground water extraction, many plains in Iran are experiencing subsidence. Among these areas, we can mention the southwestern part of Tehran, which has a large resident population and has suffered severe subsidence in the last two decades. In order to study subsidence, various ground and aerial methods are used, and the interferometric synthetic aperture radar (InSAR) system is one of those techniques that measures accurate values of ground surface displacement with high spatial resolution across a large study area. The small baseline subset (SBAS) method is a remote sensing-based technique to analyze the time series of radar interferometry. It is particularly important to examine subsidence patterns over different time frames in a geographical area and their relationship with climatic parameters, such as precipitation, in remote sensing. In this context, this research uses the SBAS method to obtain the average displacement velocity field of southwest Tehran for the period from 2014 to 2017. The maximum amount of subsidence in this area is 174 mm per year along the satellite's line of sight and 227 mm per year in the vertical direction. The time series obtained from InSAR shows the uplift during certain periods. This uplift is attributed to rainfall exceeding 20 mm before the uplift events, particularly in the last six measurements, where heavy rain has resulted in an uplift of up to 50 mm.

Keywords: subsidence, elevation, radar interferometry, SBAS, uplift, GMTSAR.

1. Introduction

Due to recent droughts, excessive harvesting, and water consumption in various fields such as agriculture, industry, and drinking water in Iran, many plains have experienced subsidence. Among these areas, we can mention the southwestern part of Tehran, which has been severely affected by the subsidence over the last two decades.

According to geological studies conducted by the Geological Survey and Mineral Exploration of Iran (GSI), the thickest sedimentary layers (more than 150 meters) that constitute the aquifer system of this region are associated with the highest subsidence rate (Dehghani et al., 2013). The storage coefficient of the southern part of the aquifer system, located in the subsidence area, is much lower than that of the northern part. This is due to the presence of large amounts of fine-grained sediments in this portion of the aquifer system (Shemshaki et al., 2005). The report from the National Cartographic Center (NCC) based on the accurate leveling network carried out from 1995 to 2000 in the region indicated a maximum subsidence rate of 200 mm per year (Arabi et al., 2005), which increased to 230 mm per year in 2005 (Amighpey et al., 2006). The high rate of subsidence threatens structures and reduces the porosity of the aquifer, thereby diminishing its ability to replenish water (Dehghani et al., 2013).

Among the various ground and space methods used to study subsidence, the interferometric synthetic aperture radar (InSAR) system is one of those techniques that provide accurate measurements of land surface displacement with high spatial resolution over a wide area (Galloway et al., 1998; Peltzer et al., 1998; Fruneau & Sarti, 2000; Tesauro et al., 2000; Crosetto et al., 2002; Motagh et al., 2007). Recent applications include Aditiya and Ito (2023), who reported subsidence rates of 100-120 mm/year in Semarang, Indonesia, using a new small baseline subset InSAR technique. Bokhari et al. (2023) found subsidence up to 92 mm/year in Gwadar, Pakistan, via PS-InSAR.

In this context, several studies have been conducted to investigate subsidence in the southwest of Tehran. Alipour et al. found the maximum subsidence between 2003 and 2005 to be approximately 225 mm per year using the small baseline subset (SBAS) technique (Alipour et al., 2008). Additionally, the maximum subsidence in the period from 2004 to 2008 was estimated to be 256 mm per year by Dehghani et al. (2013). Using an algorithm based on the combination of StaMPS and DePSI methods, Sadeghi et al. obtained a value of 249 mm per year for the years 2003 to 2008 (Sadeghi et al., 2014). Although numerous studies have been conducted to study subsidence in the southwestern region of Tehran, most of these studies were conducted before 2010. Given the severity of the crisis in this region and the irreparable damage caused by this issue, continuous studies over different periods are necessary to understand the subsidence patterns of the area. For this reason, this study investigates the subsidence of the Tehran plain in the years 2014 to 2017 using the SBAS method to process the interferometric radar time series.

2. Material and methods

2.1. InSAR

Radar sensors generate a pulse of electromagnetic energy and send it toward the target. A part of this energy is returned to the sensor from the objects in the radar's field of view, which the sensor receives, measures, and records. Radar waves propagate in the atmospheric environment (for example, through clouds, fog, smoke, and dust) without significant signal attenuation, and this enables imaging at night and in various weather conditions. The radar data recording system captures the measurements recorded by the returning waves, and the radar operates in two parts: amplitude and phase (Hanssen, 2001).

The basis of radar interferometry is the phase difference between two images taken from the same area, which leads to the production of an interferogram. The interferogram is derived from the product of one radar image and the complex conjugate of the second image. Therefore, the difference in phase between the two images forms the interferometric phase, while the product of the amplitudes of both images produces the interferometric amplitude (Hanssen, 2001):

$$y_1 = a_1 \exp(i\,\varphi_1) \tag{1}$$

$$y_2 = a_2 \exp(i\,\varphi_2) \tag{2}$$

$$y_1 \cdot y_2^* = a_1 a_2 \exp(i\,(\varphi_1 - \varphi_2)) = A \exp(i\,\phi) \tag{3}$$

In relations (1) to (3), y_1 and y_2 are the waves recorded in the first and second images for a given point, while a_1 and a_2 represent the amplitudes of the recorded waves, and φ_1 and φ_2 indicate their phase. A is the product of the amplitude of the mentioned waves, and finally, ϕ is the phase of the interferogram. The sign * the denotes complex conjugate.

In addition to displacement, other factors also affect the interferometric phase, which can be defined as a function of these factors (Kampes, 2006; Hooper, 2006; Dehghani et al., 2013; Yun et al., 2015):

$$\phi_{InSAR} = \phi_{topo} + \phi_{orb} + \phi_{defo} + \phi_{atm} + \phi_{noise} \tag{4}$$

where ϕ_{InSAR} is the interferometric phase difference between two radar images. Additionally, ϕ_{topo} is the phase caused by the topography of the region, which can be removed using a digital elevation model (DEM) (Ding et al., 2008). The phase ϕ_{orb} is produced due to the curvature of the Earth and is removed using accurate orbital information (Yun et al., 2015). The ϕ_{Noise} refers to the noise phase, mainly caused by the incoherence of the InSAR signal due to vegetation or land surface environmental changes. The Goldstein filter is also used to reduce the noise phase (Hanssen, 2001). The phase ϕ_{atm} is related to atmospheric effects. In order to correct the phase caused by the atmosphere, different methods have been proposed. The most effective way to eliminate this is to calculate it using the atmospheric parameters produced by numerical meteorological models such as ERA-Interim, WRF, and MERIS sensor products (for ENVISAT ASAR images) (Bekaert et al., 2015). The relationship between displacement phase (ϕ_{defo}) and displacement amount along the line of sight of the satellite (Δx_{LOS}) is expressed by equation (5) (Massonnet & Feigl, 1998):

$$\phi_{defo} = -\frac{4\pi}{\lambda}\Delta x_{LOS} \tag{5}$$

In the above relationship, λ is the wavelength of the transmitted signal. The displacement calculated in each interferogram is along the line of sight of the satellite, and to study the displacements of the earth's surface, this measurement should be converted into displacement in the horizontal and vertical directions. In studies related to subsidence, assuming there is no horizontal displacement, equation (6) is used to convert the value of displacement in the vertical direction (Dai et al., 2015):

$$\Delta r_{vert} = \frac{\Delta x_{LOS}}{\cos\theta} \tag{6}$$

In the above relationship, Δr_{ver} represents the height displacement, and θ is the incidence angle of the signal.

Generally, the lack of temporal and spatial correlation between the images results in a significant portion of the interferogram having a low correlation, which introduces uncertainty in the measurements. Therefore, interferometric time series analysis techniques have been proposed (Ferretti et al., 2001). Among these techniques, we can mention the permanent scatterers method and the SBAS method. The SBAS method is used in this research.

2.2. SBAS method

This method uses images of the same area at different times. Since the large spatial and temporal baseline between an image pair causes greater spatial and temporal inconsistency in the interferogram, in this method, a pair of images with a small spatial and temporal baseline is used (Berardino et al., 2002). The interferometric phase is the result of the even phase difference of its constituent images. By correcting the phase of the interferogram, the corrected phase of each pair of forming images can also be recovered. Equations of equation (7) show the corresponding linear equations for a scatterer (Berardino et al., 2002):

$$\begin{cases} \phi_1 = \phi_{12} = \varphi_1 - \varphi_2 \\ \quad\vdots \\ \phi_k = \phi_{ij} = \varphi_i - \varphi_j \end{cases} \tag{7}$$

In the above system of equations, $k = 1, \ldots, n$ and $i, j = 1, \ldots, n$ so that the n is the number of interferograms and m is the number of images. Also, ϕ_k is the k^{th} interferometric phase, ϕ_{ij} is the interferometric phase obtained from the i^{th} and the j^{th} images, φ_i is the phase of the i^{th} image, and φ_j is the phase of the j^{th} image. The above equations can be written as follows:

$$\boldsymbol{L} = \boldsymbol{AX} \tag{8}$$

where L is the observation vector, A is the matrix of coefficients, and X is the vector of unknowns, each defined as follows (Berardino et al., 2002):

$$\mathbf{L}_{(n\times 1)} = \begin{bmatrix} \phi_1 \\ \phi_2 \\ \vdots \\ \phi_n \end{bmatrix}, \mathbf{X}_{(m\times 1)} = \begin{bmatrix} \varphi_1 \\ \varphi_2 \\ \vdots \\ \varphi_m \end{bmatrix}, \mathbf{A}_{(n\times m)} = \begin{bmatrix} 1 & -1 & \cdots & 0 \\ 0 & 1 & \cdots & 0 \\ . & . & \cdots & . \\ 0 & 0 & \cdots & 1 \end{bmatrix} \tag{9}$$

In this method, the phase of the first image is considered equal to zero as a reference. In fact, the phases of the other images are determined relative to the first image. As a result, the vector of unknowns is expressed as follows:

$$\varphi_1 = 0 \quad , \quad \mathbf{X}_{(m-1\times 1)} = \begin{bmatrix} \varphi_2 \\ \varphi_3 \\ \vdots \\ \varphi_m \end{bmatrix} \tag{10}$$

Finally, the vector of unknowns is estimated using the least squares method as follows:

$$\mathbf{X} = (\mathbf{A}^t\mathrm{B}) - 1\mathbf{A}^t\mathrm{B} \tag{11}$$

Considering the phase of the first image to be zero, in order to solve the above equation, the condition regarding the number of images and the number of interferograms must be met as $n \geq m - 1$. By estimating the corrected value of the phase of the images, it is possible to obtain the height changes (corresponding to the phase changes) between any two desired images that are in the same grid (Berardino et al., 2002).

2.3. Processing steps

In this research, GMTSAR was used to process radar images. This collection is based on accurate orbital data and uses the GMT tool for image processing (Sandwell et al., 2011).

The steps of producing an interferogram with GMTSAR include: the selection of the main image, pre-processing to convert files containing phase and amplitude information from each sensor's specific format into ASCII and raw files, production of SLC images, geometric registration of the main and slave images, formation of an interferogram, correction of the Earth's curvature effect (orbital effect or flat earth using the exact orbital position of the satellite), topography correction (using SRTM DEM model with horizontal spatial resolution of 90 meters), filtering to reduce phase noise, phase recovery with the SNAPHU algorithm, and finally, conversion to s geographic coordinate system (Fig. 1).

The selection of the main image in the case where interferograms are created with respect to a common main image is based on the cumulative coherence of all interferograms (Kampes, 2006), which is a function of the vertical baseline $B_\perp$, time baseline T, and Doppler center frequency f_{dc} according to the following equation:

$$\gamma^m = \frac{1}{k}\sum_{k=1}^{K}[g(B_\perp^{k,m}, B_{\perp,\max}).g(T^{k,m}, T_{\max}).\mathrm{g}(f_{dc}^{k,m}, f_{dc,\max})] \tag{12}$$

where the function g is defined as follows:

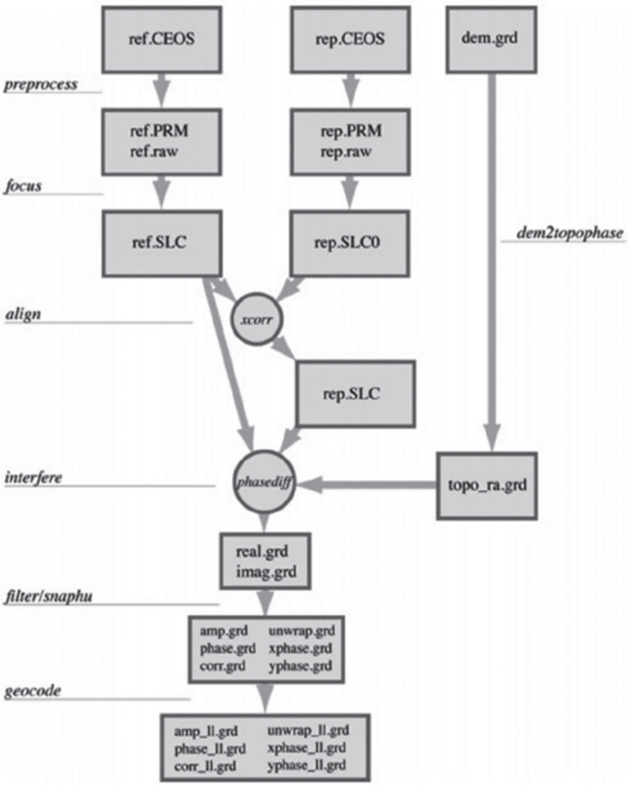

Figure 1. Flowchart of interferogram production by GMTSAR (Sandwell et al., 2011)

$$g(x,c)=\begin{cases}1-\dfrac{|x|}{c} & for\,|x|\le c\\ 0 & for\,|x|>c\end{cases} \tag{13}$$

In this regard, the cumulative coherence γ^m is for the m^{th} base image, and k is the number of slave images. In this study, the image from 12/02/2016 was selected as the main image. In order to generate a displacement velocity field by the SBAS time series method, 45 interferograms were formed using the available images. The graph related to the generated interferograms is shown in Figure 2. In this network, the red circles correspond to the images, and the black lines indicate the interpolation consisting of two images. In the network formed for the SBAS method, all the interferograms must be connected to each other as a continuous network, and there should be no separation between an interferogram and the network composed of other interferograms, so that the problem can be solved without any lack of order.

Atmospheric correction of the interferometric phase, as an effective source of error, was performed using the meteorological parameters of the ECMWF global model. In the ECMWF model, the final model is produced in the form of ERA-Interim data by using prediction models and the data measured by various sensors, including radiosonde, synoptic stations, satellite data, tide gauges, information

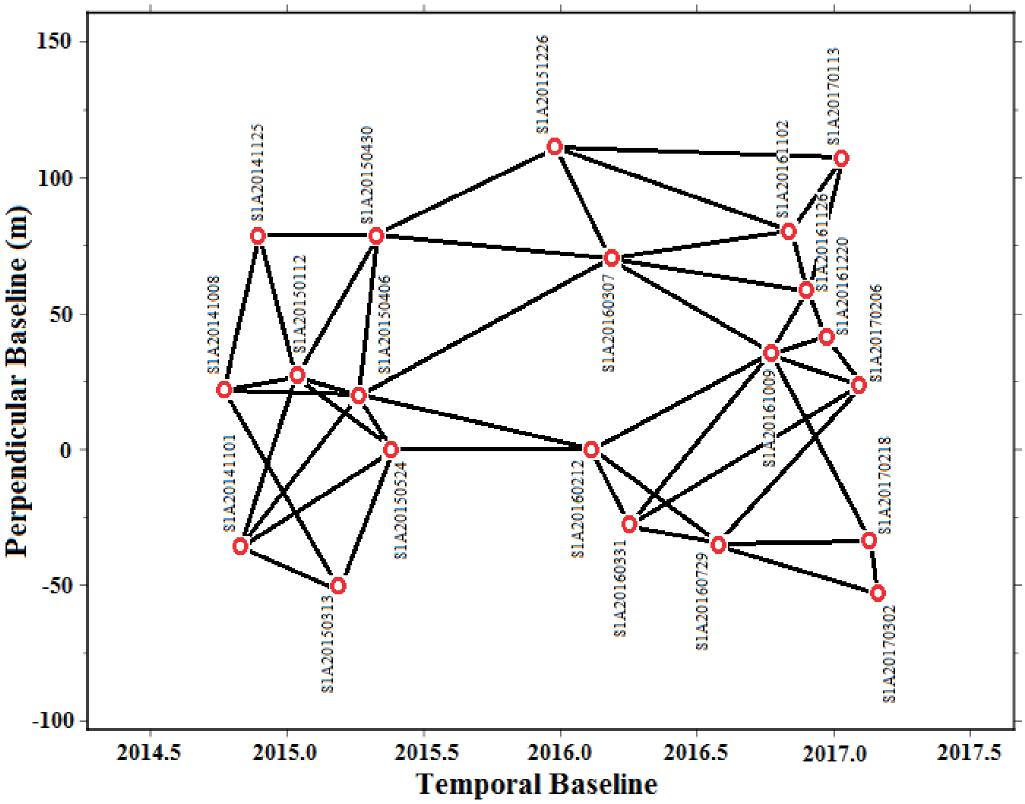

Figure 2. Graph composed of interferograms for SBAS time series processing

collected by ships, and other meteorological sources. The purpose of data mining in this model is to estimate the best atmospheric condition using short-term data. This numerical meteorological model provides users with atmospheric parameters in 37 pressure layers in the vertical direction and with various horizontal spatial resolutions using meteorological observations (https://www.ecmwf.int/en/about). In this study, data with a spatial resolution of 0.125 degrees were used. In order to calculate the tropospheric delay in the vertical direction, the following relationship related to microwave waves was used (Davis et al., 1985):

$$ZTD = 10^{-6} \sum_{i=surface}^{last\ layer} \left(\left(k_1 R_d \left(\frac{P_i - e_i}{R_d T_i} + \frac{e_i}{R_w T_i} \right) + \left(k_2{}' \frac{e_i}{T_i} + k_3 \frac{e_i}{T_i^2} \right) \right) dh_i \right) \quad (14)$$

In this regard, e_i, p_i, and T_i represent water vapor density, temperature, and pressure in the desired layer, respectively. It should be noted that another atmospheric parameter effective in tropospheric delay is liquid water ($1.4W_i$) (Hanssen, 2001), which was considered in this research to calculate tropospheric delay. All these parameters are provided by ERA-Interim. Then, the following mapping function was used to estimate the tropospheric delay in the inclined direction:

$$mf = \frac{1}{\cos\theta} \quad (15)$$

In this regard, θ is the viewing angle of the satellite. After the tropospheric correction of the interferograms, the SBAS algorithm available in GMTSAR was used to generate the displacement velocity field.

3. Dataset

In this research, 21 low-pass SENTINEL-1A images from October 2014 to March 2017 with a central viewing angle of 39.955 degrees were used. The SENTINEL-1A satellite has been in operation since 2014 and passes over an area every 12 days to gather data. It should be noted that with the launch of the SENTINEL-1B satellite in 2016, the time resolution of taking images of this satellite has been increased to 6 days. Due to its precise orbital design and regular orbital movement, this sensor has less orbital displacement during repeated passes of the same area, and accordingly, the interferograms formed from the images taken by it have a shorter baseline length (less than 150 meters). In terms of timing, it captures images more regularly than the ENVISAT satellite. It should also be noted that SENTINEL-1A images include three wide interferometry ranges: IW1, IW2, and IW3, which cover a broad area. However, in this study, only the IW2 range is used due to the location of the study area (Fig. 3).

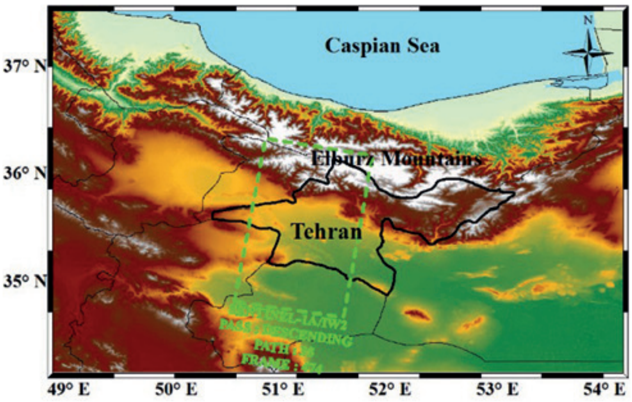

Figure 3. IW2 wide area coverage status of SENTINEL-1A images

4. Analysis of the results

The displacement velocity field obtained from the SBAS method (Fig. 4a) for the period from 2014 to 2017 shows subsidence with a maximum value of 174 mm per year along the line of sight of the satellite for the southwestern region of Tehran. Assuming no horizontal displacement and using relation (6), the maximum amount of subsidence in the vertical direction is equal to 227 mm per year.

Most of the subsidence areas are located in Shahryar and Islamshahr cities, which seriously threaten urban areas and communication routes. According to the research, the reason for this amount of subsidence is related to drought and excessive harvesting of existing wells in the region. In this area, 6,848 wells have been dug for drinking, agricultural, industrial, and other purposes, with the largest share of consumption attributed to the agricultural sector, which uses 480.14 million cubic meters per year (Geological Survey and Mineral Exploration of Iran, 2020). Figure 5 shows a three-dimensional representation of the region's subsidence, indicating that the amount of subsidence is significantly higher compared to neighboring areas, posing a serious threat to the region.

The time series of displacement in the subsidence area from October 2014 to March 2017 is shown in Figure 6. As can be seen, with the passage of time, the subsidence part shows itself and approaches the red color. Due to the indiscriminate extraction of underground water, the dominant displacement of the area is related to subsidence and reaches more than 300 mm in the studied time period. Notably, on some dates, the subsidence part (which tends towards green, yellow, and red colors) has become fainter compared to the previous date (it tends towards blue), indicating an uplift. For example, the subsidence in the displacement field for the date 2016-02-12 is weaker compared to the previous date. Additionally, the highest amount of subsidence was recorded on 2016-11-02,

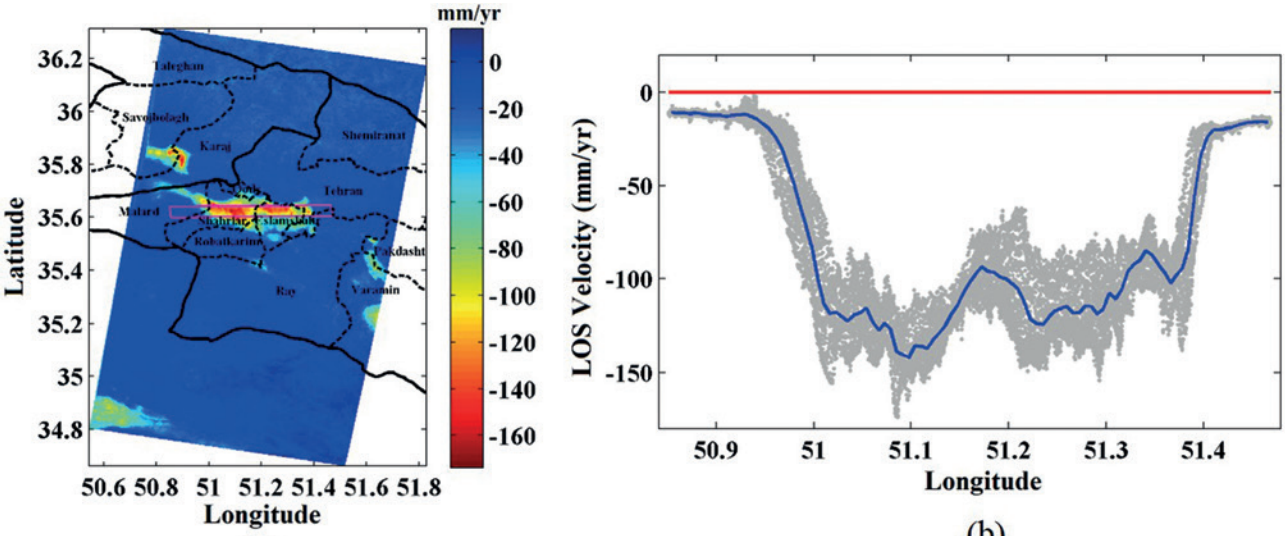

(a) (b)

Figure 4. (a) The field of the average movement speed along the line of sight of the satellite, (b) Drawing the average movement speed of the points in the rectangle in purple color

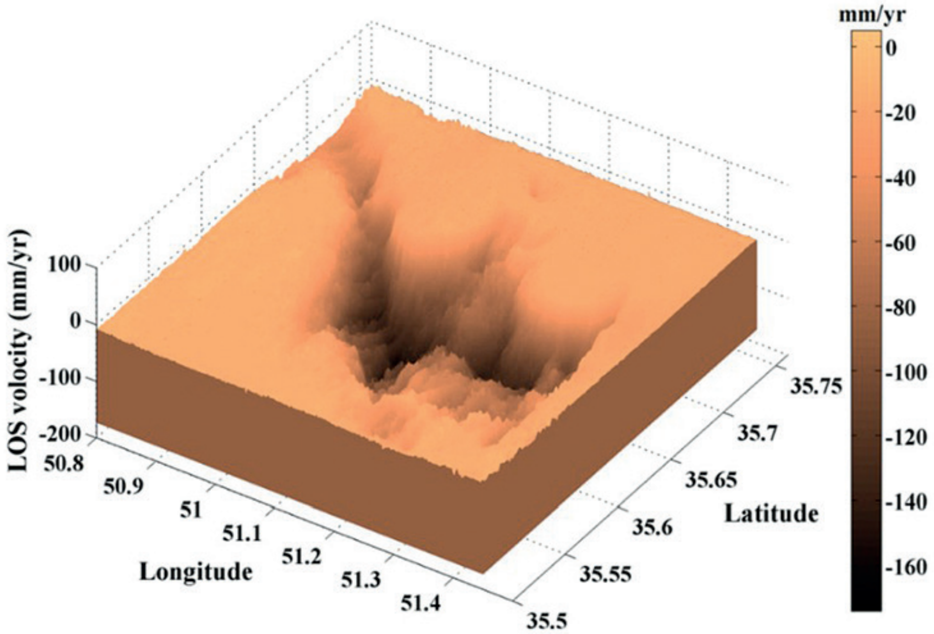

Figure 5. Three-dimensional representation of the field of the average displacement speed of the study area

after which (over the last six dates) the red areas became fainter, suggesting an uplift at this time.

For a better investigation, since the cause of subsidence in the region is the lowering of the underground water level, which is closely related to precipitation in the region, the monthly average precipitation from Shahryar station (the closest station to the subsidence area) was evaluated alongside the time series of regional displacement (Fig. 7).

The comparison of the time series of area displacement and the average monthly precipitation shows that during months when precipitation exceeds 20 mm, the area experiences uplift after a period of approximately one month (for the water from the rainfall to join the underground water table). This trend is particularly evident in the last six dates due to heavy rainfall, resulting in up to a 50 mm rise. This indicates that the area can return to its original state and react quickly to the increase in underground water storage.

This information could be valuable in preventing the crisis caused by subsidence in the region. However, it should also be noted that, in addition to precipitation amounts,

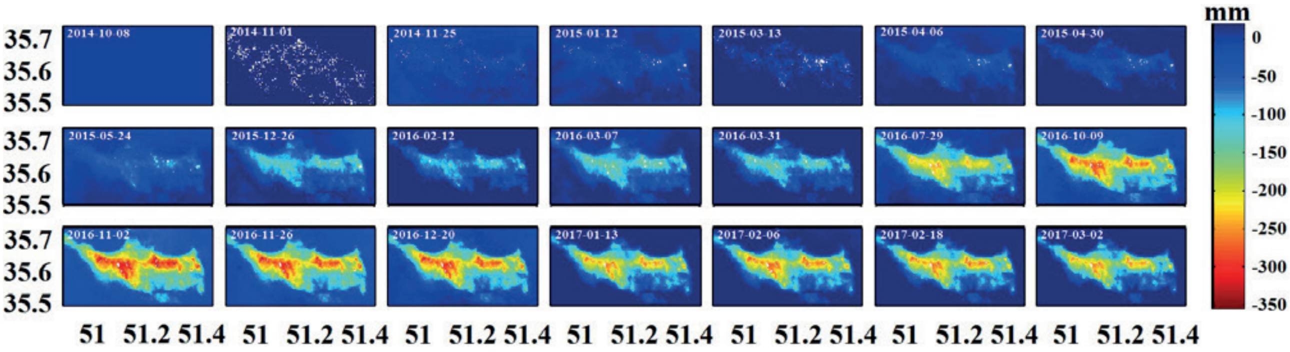

Figure 6. Time series of displacement along the line of sight of the satellite

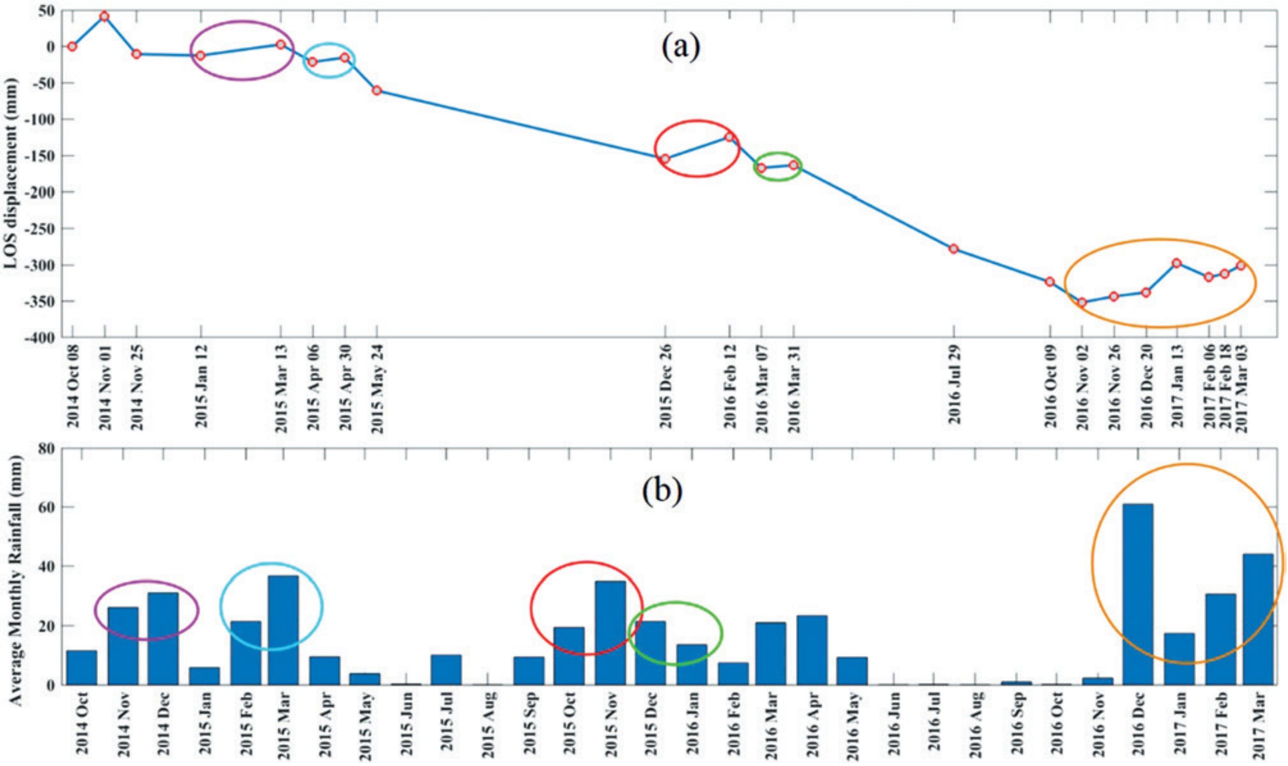

Figure 7. (a) Time series of displacement of the subsidence area along the line of sight of the satellite, (b) Bar chart of monthly rainfall of Shahriar station

the relationship between underground water extraction and area displacement should be investigated to achieve comprehensive knowledge.

4. Conclusion

In this study, 21 SENTINEL-1A radar images from October 2014 to March 2017 were used to calculate the displacement velocity field in the southwestern region of Tehran to investigate the subsidence phenomenon of this region. The obtained results indicate a maximum subsidence of 174 mm per year along the line of sight of the satellite and 227 mm in the vertical direction. The time series of displacement for the region indicates subsidence of more than 300 mm during this period; however, in some instances, it also shows uplift. Examining the amount of monthly rainfall of Shahriar station alongside the time series of the displacement of the area reveals that when the amount of rainfall exceeds 20 mm, the area experiences an uplift after a time interval of approximately one month. In the last six dates of the mentioned time series, an increase of about 50 mm is observed. This information can provide valuable insights into the displacement pattern of the region in order to prevent the emerging crisis. It should be noted that the amount of water extraction from underground wells should also be considered. In other words, with the information obtained from the displacement pattern, the amount of precipitation, and the amount of water extraction, appropriate measures can be provided to address the subsidence problem of the region. To address subsidence, practical measures include:

Regulating groundwater extraction: Limiting water withdrawals from groundwater wells, especially during periods of low rainfall, to reduce subsidence rates, informed by real-time displacement and rainfall data.

Enhancing groundwater recharge: Implementing artificial recharge techniques, such as rainwater harvesting and injection wells, to restore aquifer levels, especially after rainfalls exceeding 20 mm.

Land use planning: Restricting heavy construction in areas of high subsidence identified by the displacement velocity field to minimize structural risks.

Monitoring and policy integration: Establishing a continuous monitoring system using SENTINEL-1A data to track subsidence and uplift patterns, integrating findings with precipitation and extraction data to inform adaptive water management policies.

Future studies should analyze subsidence patterns over additional time periods and correlate them with precipitation and water extraction data to refine these mitigation strategies.

Acknowledgements

The authors of this article are grateful to the European Space Agency (ESA), the European Centre for Medium-Range Weather Forecasts (ECMWF), and the National Meteorological Organization, respectively, for providing SENTINEL-1A radar images, ERA-Interim atmospheric parameters, and monthly precipitation data for free.

References

Aditiya A., & Ito T., 2023, Present-day land subsidence over Semarang revealed by time series InSAR new small baseline subset technique. International Journal of Applied Earth Observation and Geoinformation 125, 103579. https://doi.org/10.1016/j.jag.2023.103579.

Alipour S., Motgah M., Sharifi M., & Walter T., 2008, InSAR time series investigation of land subsidence due to groundwater overexploitation in Tehran, Iran. Paper presented at the Second Workshop on Use of Remote Sensing Techniques for Monitoring Volcanoes and Seismogenic Areas, 2008. USEReST 2008. Availabale on: https://ieeexplore.ieee.org/abstract/document/4740370

Amighpay M., Arabi S., Talebi A., & Djamour Y., 2006, Elevation changes of the precise leveling tracks in the Iran leveling network. Scientifc report published in National Cartographic Center (NCC) of Iran.

Arabi S., Montazerian A.R., Maleki E., & Talebi A., 2005, Study of land subsidence in south-west of Tehran. Journal of Engineering and Surveying 69: 14–24.

Bekaert D., Walters R., Wright T., Hooper A., & Parker D., 2015, Statistical comparison of InSAR tropospheric correction techniques. Remote Sensing of Environment 170: 40–47.

Berardino P., Fornaro G., Lanari R., & Sansosti E., 2002, A new algorithm for surface deformation monitoring based on small baseline differential SAR interferograms. IEEE Transactions on Geoscience and Remote Sensing 40(11): 2375–2383.

Bokhari Rida, Hong Shu, Aqil Tariq, Nadhir Al-Ansari, Rufat Guluzade, Ting Chen, Ahsan Jamil, & Muhammad Aslam, 2023, Land subsidence analysis using synthetic aperture radar data. Heliyon 9(3). https://doi.org/10.1016/j.heliyon.2023.e14690.

Crosetto, M., Tscherning, C. C., Crippa, B., & Castillo, M. (2002). Subsidence monitoring using SAR interferometry: reduction of the atmospheric effects using stochastic filtering. Geophysical Research Letters 29(9), 1312. 10.1029/2001GL013544, 2002.

Dai K., Liu G., Li Z., Li T., Yu B., Wang X., & Singleton A., 2015, Extracting vertical displacement rates in Shanghai (China) with multi-platform SAR images. Remote Sensing 7(8): 9542–9562.

Davis J., Herring T., Shapiro I., Rogers A., & Elgered G., 1985, Geodesy by radio interferometry: Effects of atmospheric modeling errors on estimates of baseline length. Radio Science 20(6): 1593–1607.

Dehghani M., Zoej M.J.V., Hooper A., Hanssen R.F., Entezam I., & Saatchi S., 2013, Hybrid conventional and Persistent Scatterer SAR interferometry for land subsidence monitoring in the Tehran Basin, Iran. ISPRS Journal of Photogrammetry and Remote Sensing 79: 157–170.

Ding X.-l., Li Z.-w., Zhu J.-j., Feng G.-c., & Long, J.-p., 2008, Atmospheric effects on InSAR measurements and their mitigation. Sensors 8(9): 5426–5448.

Ferretti A., Prati C., & Rocca F., 2001, Permanent scatterers in SAR interferometry. IEEE Transactions on Geoscience and Remote Sensing 39(1): 8–20.

Fruneau B., & Sarti F., 2000, Detection of ground subsidence in the city of Paris using radar interferometry: isolation of deformation from atmospheric artifacts using correlation. Geophysical Research Letters 27(24): 3981–3984.

Galloway D.L., Hudnut K.W., Ingebritsen S., Phillips S.P., Peltzer G., Rogez F., & Rosen P., 1998, Detection of aquifer system compaction and land subsidence using interferometric synthetic aperture radar, Antelope Valley, Mojave Desert, California. Water Resources Research 34(10): 2573–2585.

Geological Survey and Mineral Exploration of Iran, 2020, The report on the investigation of the risks caused by land subsidence in Tehran province, the geological water report of the land subsidence area in the southwest of the Tehran plain, underground water balance. Availabale on: www.ngdir.ir/.

Hanssen R.F., 2001, Radar interferometry: data interpretation and error analysis (Vol. 2). Springer Science & Business Media.

Hooper A.J., 2006, Persistent scatter radar interferometry for crustal deformation studies and modeling of volcanic deformation. Stanford University.

Kampes B., 2006, Radar interferometry: Persistent scatterer technique. The Netherlands, Springer.

Massonnet D., & Feigl K.L., 1998, Radar interferometry and its application to changes in the Earth's surface. Reviews of geophysics 36(4): 441–500.

Motagh M., Djamour Y., Walter T.R., Wetzel H.-U., Zschau J., & Arabi S., 2007, Land subsidence in Mashhad Valley, northeast Iran: results from InSAR, levelling and GPS. Geophysical Journal International 168(2): 518–526.

Peltzer G., Rosen P., Rogez F., & Hudnut K., 1998, Poroelastic rebound along the Landers 1992 earthquake surface rupture. Journal of geophysical research: solid earth 103(B12): 30131–30145.

Sadeghi Z., Valadanzouj M., & Dehghani M., 2014, Hybrid of Two Persistent Scatterer Interferometry Methods in Order to Subsidence Monitoring. Scientific Quarterly Journal of Geosciences 23(90): 45–54. Doi: 10.22071/gsj.2014.43906

Sandwell D., Mellors R., Tong X., Wei M., & Wessel P., 2011, GMTSAR: An insar processing system based on generic mapping tools. Scripps Institution of Oceanography Technical Report, UC San Diego, https://escholarship.org/uc/item/8zq2c02m

Shemshaki A., Blourchi M.J., & Ansari F., 2005, Investigating Earth subsidence at Tehran plain-Shahriar (first report). Ministry of industries and mines, geological survey of Iran. Availabale on: https://irangeomorphology.ir/

Tesauro M., Berardino P., Lanari R., Sansosti E., Fornaro G., & Franceschetti G., 2000, Urban subsidence inside the city of Napoli (Italy) observed by satellite radar interferometry. Geophysical Research Letters 27(13): 1961–1964.

Yun Y., Zeng Q., Green B.W., & Zhang F., 2015, Mitigating atmospheric effects in InSAR measurements through high-resolution data assimilation and numerical simulations with a weather prediction model. International Journal of Remote Sensing 36(8): 2129–2147.